Industrial Chemistry & Materials

ROYAL SOCIETY OF CHEMISTRY

PAPER

View Article Online
View Journal

Check for updates

Cite this: DOI: 10.1039/d5im00320b

Rapid photoprinting of piezoelectric solid polymer electrolytes for scalable structural energy storage composites

Žan Simon, †*[a] Timothy Harte, †[ab] Anna Demeraux,[a] Ben Newman,[a] Piers Coia,[a] Nilupuli C. Rathnayaka,[a] Daniel J. Eyckens,[b] Bhagya Dharmasiri *[a] and Luke C. Henderson *[a]

3D printing of solid polymer electrolytes (SPEs) offers a scalable platform for fabricating intricate architectures whilst maintaining the desired electrochemical and mechanical properties. Here, we present an innovative approach for the fabrication of bicontinuous SPEs, containing an ion-conductive solvate ionic liquid (SIL) network within a mechanically reinforcing polymer, *via* photopolymerisation using masked stereolithography (MSLA). Compared to mould-cured (bulk) SPEs of identical composition, the additively manufactured samples exhibited superior homogeneity and enhanced electrochemical and mechanical performance, attributed to the uniform phase distribution and controlled microstructure enabled by additive manufacturing. Additionally, these samples also displayed piezoelectric properties, with a linear correlation between generated current/potential and applied pressure, highlighting their applicability in energy harvesting and sensing applications. Building on this, we further demonstrate the potential of this rapid prototyping process for structural energy storage by directly printing the SPE onto carbon fibre, functionalised with a redox-active 2,6-diaminoanthraquinone, and viability of a separator-less structural supercapacitor with a snap-fit interlocking polymer electrolyte design as a proof of concept for rapid prototyping of load-bearing energy storage devices.

Keywords: Masked stereolithography; Solid polymer electrolyte; Piezoelectric energy harvesting; Carbon fibre; Industrial materials design; Rapid prototyping.

Received 7th November 2025,
Accepted 15th January 2026

DOI: 10.1039/d5im00320b

rsc.li/icm

Open Access Article. Published on 29 January 2026. Downloaded on 4/27/2026 7:11:15 PM.
This article is licensed under a Creative Commons Attribution-NonCommercial 3.0 Unported Licence.

1 Introduction

Structural energy devices represent a prominent focus in materials' research, imparting multifunctionality through careful selection of constituents in composite materials. Structural energy storage composites are materials that carry load whilst also storing charge and are central to this shift.[1–9] However, this push now demands not only multifunctionality but also rapid, scalable manufacturing. Solid polymer electrolytes (SPEs) are a key enabling component,[10] because they simultaneously reinforce the structure and provide the ionic conductivity required for charge/discharge. Resin chemistry, ionic liquid choice, filler content, and processing route all determine the SPE's combined mechanical and electrochemical performance.[11–16] Bicontinuous SPE architectures are especially promising, since a continuous, load-bearing polymer matrix coexists with an interpenetrating, ion-conducting pore network created *via* the polymerisation-induced microphase separation (PIMS) method. These structures can deliver the balance of stiffness and ion transport required for real-world structural cells.[17–19] Using widely available epoxies (*e.g.*, Hexion RIM R935/H936) together with easily synthesised solvate ionic liquids (SILs) produces a more practical, lower-cost, and recyclable route to bicontinuous SPEs, making this combination well suited to industrial-scale deployment.[20,21] However, a critical manufacturing bottleneck remains. Ionic liquids and SILs can accelerate epoxy curing by up to 20 times, collapsing the processing window and forcing very rapid gelation.[22,23] That speed limits thorough mixing, degassing, and impregnation steps, increasing void formation and degrading electrochemical performance by introducing discontinuity. To translate bicontinuous SPEs from lab-scale demonstrations to high-throughput production, strategies that accommodate or control this accelerated cure are essential. Rapid

[a] *Institute for Frontier Materials, Deakin University, Waurn Ponds, Victoria 3216, Australia. E-mail: zsimon@deakin.edu.au, k.dharmasiri@deakin.edu.au, luke.henderson@deakin.edu.au*
[b] *Manufacturing, Commonwealth Scientific and Industrial Research Organisation, Clayton, Victoria 3168, Australia*
† These authors contributed equally to this work.

© 2026 The Author(s). Co-published by the Institute of Process Engineering, Chinese Academy of Sciences and the Royal Society of Chemistry

Open Access Article. Published on 29 January 2026. Downloaded on 4/27/2026 7:11:15 PM.
This article is licensed under a Creative Commons Attribution-NonCommercial 3.0 Unported Licence.

manufacturing solutions must be developed to preserve both structural integrity and electrochemical function at scale, such as tailoring the cure kinetics, continuous mixing and degassing systems, or modifying formulations that decouple curing and preserve ionic conductivity. Research has already shown fully 3D direct-ink-written (DIW), shape-versatile Li-ion batteries using rheological optimisation of printable inks for solid current collectors and electrodes. Relying on photocurable, reinforced, PDMS-based gel polymer electrolytes for high-throughput extrusion enabled free-form, customizable power source fabrication.[24] DIW was also used to fabricate ceramic and hybrid all-solid-state electrolytes in arbitrary shapes while retaining high ionic conductivity, which printed free-standing geometries and direct printing onto LFP cathodes.[25] However, the main challenges of DIW for energy storage revolve around balancing printable ink rheology with electrochemical performance and ensuring uniformity and reproducibility across large runs. Together these create difficulties in maintaining strong interfacial adhesion and mechanical integrity of printed stacks, and meeting required post-processing (curing, drying, sintering) without distorting free-form parts. Additionally, long-term stability, safety, and the need for customized industrial printers and environmental controls present hurdles compared to established manufacturing methods.[26]

Recent reports also detail the development of customised SPEs using additive manufacturing processes that optimise the electrochemical efficiency of energy storage systems like supercapacitors and batteries.[27–30] This approach enables the creation of complex and intricate geometries that are otherwise challenging to achieve with traditional manufacturing methods, paving the way for large scale manufacturing of structural energy storage composites. Among the diverse methods of additive manufacturing, photopolymerisation presents as a particularly effective technique for the swift production of SPEs with enhanced electrochemical and mechanical performance.[31,32] Cheng *et al.*[30] improved the printability and electrochemical performance of polyethylene-oxide-based composite polymer electrolytes for energy storage devices by incorporating silane-treated hexagonal boron nitride (S-hBN) platelets into the polymer matrix, enhancing both the ionic conductivity and thermal management properties. Zekoll *et al.*[33] used SLA printing to create $Li_{1.4}Al_{0.4}Ge_{1.6}(PO_4)_3$-based hybrid electrolytes with intricate 3D architectures, enhancing both ionic conductivity and mechanical properties through topography optimisation. McOwen *et al.*[32] developed lithium lanthanum zirconium oxide-based inks for conformal, dendrite resistant SPEs, demonstrating how controlled microstructures provide a pathway for improved ion transport and performance in lithium–metal batteries. In general, research limitations in the field of electrolyte manufacture lie in the development of printable electrolytes that can function immediately when used in an energy storage device for rapid prototyping. Additionally, gaps remain in the understanding of the microstructure of these electrolytes, particularly regarding the inter- and intralayer ion transport and pore formation during photocuring in relatively thick (*i.e.*, 50 μm) layers. Thus, optimising the microstructure for reproducibility and scalability remains an area that demands more exploration.[27,28,30,32]

When using an ionic liquid as the liquid phase in these SPEs, an intriguing phenomenon was also reported recently, wherein a liquid-to-crystalline phase transition occurs under relatively low pressures, which results in a pressure-dependent electric potential response.[34,35] Thus, opening pathways of imparting a third function to these structures (*i.e.*, load bearing due to inherent strength of CF, energy storage, and energy generation and harvesting in one). Previous studies have shown some ILs can form crystal structures under compression,[36] with some only displaying crystal polymorphism during decompression.[37] Phase behaviour of ILs under applied external pressure has been investigated before, with Yoshimura *et al.*[36] observing vibrational changes in the CH stretching spectrum above 4 GPa, using IL containing *N*,*N*-diethyl-*N*-methyl-*N*-(2-methoxyethyl)ammonium (DEME) cation and TFSI anion. No crystallisation was observed up to 5.5 GPa. When using 1-butyl-3-methylimidazolium iodide IL, Takekiyo *et al.*[38] observed pressure-induced partial crystallisation from the glassy state. Su *et al.*[39] also monitored reversible crystallisation *in situ* with the same cation, but a different anion ([BMIM][PF_6]), leading to the conclusion that liquid-to-crystalline phase transition in ILs and its subsequent, recently identified piezoelectric effect in ILs is pressure-dependant, as well as inextricably linked to the molecular signature. Multiple phase transitions have been detected before and even crystallisation under extreme pressure conditions.[37,39] However, such pressures are prohibitively large for scalable energy harvesting. It was also recently shown that the neat [Li-G3]TFSI SILs (a subset of ILs) displayed a similar piezoelectric effect imparted by liquid-to-crystalline phase transition following pressurisation, with this phenomenon also observed in SPEs, where [Li-G3]TFSI is embedded within an epoxy-based resin system.[40] To further explore this property, the piezoelectric energy-generation effect of additively manufactured SPEs developed in this study has been systematically investigated. The ability of MSLA approach to precisely tailor the microstructure is anticipated to yield a more consistent and enhanced piezoelectric response. Building on this, we also demonstrate the utility of this approach by directly printing the SPE onto the surface of CF, pioneering the first reported separator-less structural energy storage device using CF as electrodes as a proof of concept for rapid prototyping structural supercapacitor concept. This approach not only eliminates the use of a separator in these structural supercapacitors, reducing the manufacture time, but also introduces a novel interlocking design, akin to Lego® blocks, where positive and negative interlocking SPE enhance structural integrity and connectivity. Furthermore, we characterise the thermal, electrochemical, and mechanical properties of photocured SPEs, both when bulk cured and additively manufactured, demonstrating the feasibility of this method for next-generation energy storage applications. This approach enhances both the structural and functional performance of SPEs, paving the way for their integration into advanced materials that can generate,

© 2026 The Author(s). Co-published by the Institute of Process Engineering, Chinese Academy of Sciences and the Royal Society of Chemistry

Open Access Article. Published on 29 January 2026. Downloaded on 4/27/2026 7:11:15 PM. This article is licensed under a Creative Commons Attribution-NonCommercial 3.0 Unported Licence.

store and release electrical energy whilst simultaneously contributing to load bearing performance.

2 Results and discussion

This study systematically explored the development of an SPE, incorporating [Li(G3)][TFSI] SIL within a photocurable resin, containing bisphenol A ethoxylate dimethacrylate monomer and 4-acryloylmorpholine as a crosslinking agent. As an initial step, the photocuring behaviour of SIL-containing resin formulations at varying ratios were investigated within conventional moulds to evaluate their mechanical properties, ionic conductivity, and morphology to determine viability as an SPE. Building upon these findings, identical compositions were subsequently fabricated using an MSLA resin printer to produce standard test coupons, allowing direct comparison between mould-cured and additively manufactured samples. Based on this comparative analysis, optimal formulations and process parameters were identified (see 4.9) and applied to print the SPE directly onto commercial CF fabric (Fig. 1). This approach seamlessly integrates the electrolyte layer with the CF electrodes, paving the way towards advanced structural supercapacitor devices that have the potential for manufacture at scale. In the following sections, all samples are referred to using a consistent nomenclature that reflects their formulation and processing method (Fig. 1).

2.1 Bulk photocuring of SPEs in moulds

As a proof of concept, the photocurable resin was initially blended with varying amounts of the SIL to assess if an SPE with both ionic conductivity and mechanical integrity could be fabricated, or if the SIL suppressed photopolymerisation. Thus, a comprehensive evaluation of the mould-cured SPEs was undertaken, including their mechanical, electrochemical, and thermal performance. SIL contents exceeding 55 wt% were employed to ensure the percolation threshold necessary for the formation of a continuous, interconnected ionic network within the polymer matrix *via* PIMS. As the SIL content increases from 55% to 90%, the ionic conductivity steadily improves from 7.33×10^{-3} mS cm^{-1} at 55% SIL to 7.83×10^{-1} mS cm^{-1} at 90% SIL, due to the growing presence of liquid, conductive domains within the bicontinuous polymer matrix (Table S1, Fig. 2), approaching the ionic conductivity of the neat SIL, which was evaluated at 8.98×10^{-1} mS cm^{-1}.[41] However, this enhancement in ion transport comes at the expense of mechanical integrity, as evinced by the depression of flexural modulus from 8.28 ± 1.50 MPa at 55% SIL to just 0.30 ± 0.11 MPa at 90% SIL (Table S3, Fig. 2), behaving more like a highly viscous gel.[41] These opposing trends reflect the

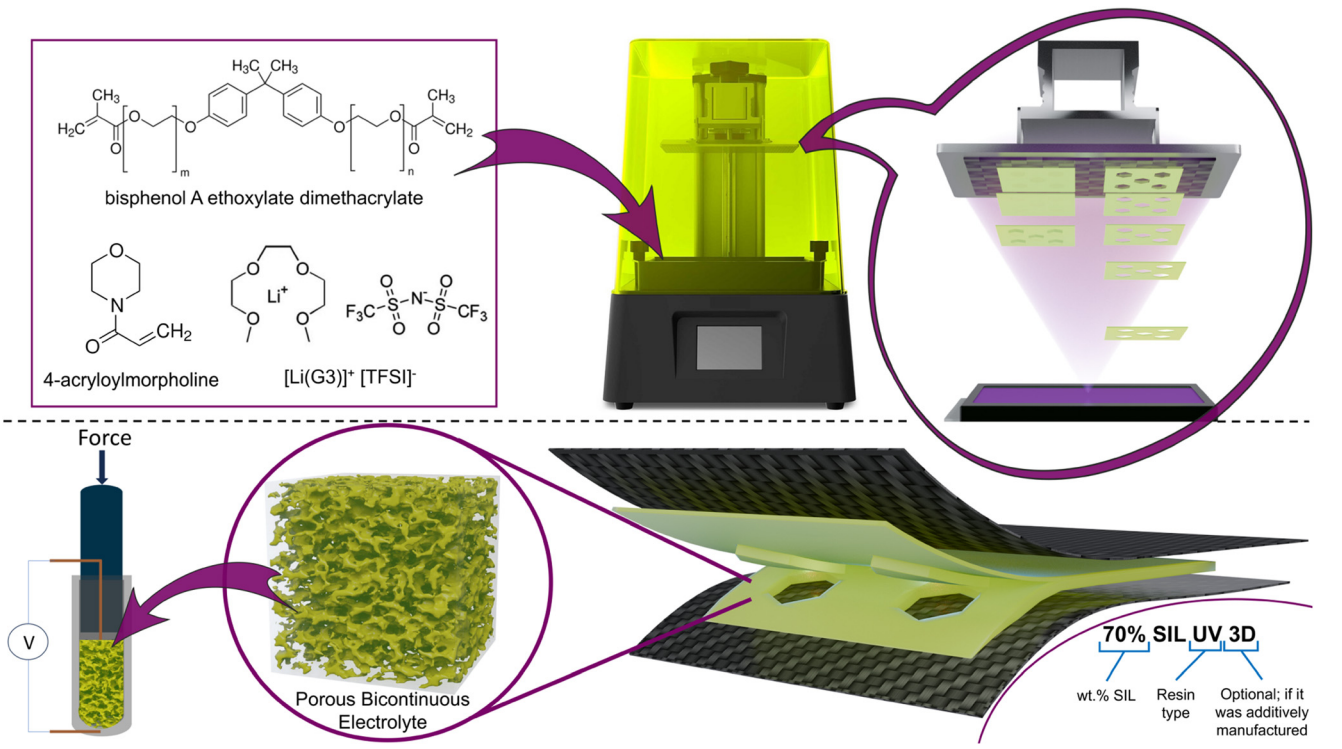

Fig. 1 Flow of investigation, including the sample naming convention. The resin, containing bisphenol A and ACMO monomers, was mixed with the solvate ionic liquid (top left) and printed using the masked stereolithography approach in 50 μm layers directly on a CF woven mat attached to the aluminium holder of the printer side-by-side. Sections with printed porous bicontinuous electrolyte on the CF (resulting in two electrodes) were cut and assembled by aligning the interlocking hexagonal shapes, which formed the separator-less supercapacitor device. Separately, the SPE was tested for its piezoelectric output using a custom setup based on the schematic in the bottom left corner.

© 2026 The Author(s). Co-published by the Institute of Process Engineering, Chinese Academy of Sciences and the Royal Society of Chemistry

Open Access Article. Published on 29 January 2026. Downloaded on 4/27/2026 7:11:15 PM.
This article is licensed under a Creative Commons Attribution-NonCommercial 3.0 Unported Licence.

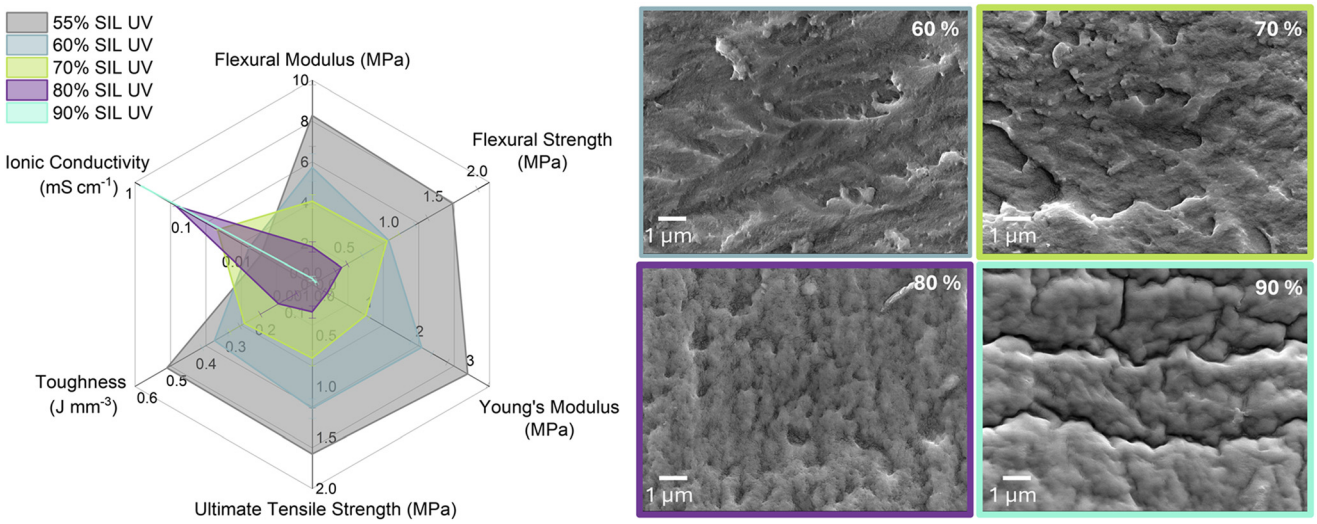

Fig. 2 A radar chart showing the flexural, tensile and compressive mechanical properties, and ionic conductivity of bulk cured SPEs. Values and detailed explanation available in the SI. SEM images are showing the microstructure of bulk cured SPEs at varying wt% ratios, from 60% to 90%.

fundamental trade-off in SPE design, increasing SIL content enhances ionic mobility by introducing more fluid, conductive domains but compromises structural cohesion due to reduced resin content. Conversely, lower SIL content favours mechanical robustness but limits ionic transport, highlighting the critical balance needed in tailoring SPEs for structural energy storage applications.

SEM micrographs reveal a relative increase in the overall porosity with rising SIL content from 60% to 80% (Fig. 2). However, the pore morphology is heterogeneous, exhibiting a broad distribution of pore sizes including both nanopores and larger voids. Notably, the SIL was removed prior to imaging, and in the case of 90% SIL sample, substantial shrinkage occurred upon SIL extraction resulting in a distinctly wrinkled surface morphology, indicating a collapsed pore structure and deformation of the polymer matrix.

2.2 Additive manufacturing of SPEs *via* MSLA

The radar chart (Fig. 3a) illustrates the variation in mechanical properties and ionic conductivity with increasing SIL content. Only 60, 70, and 80 wt% of SIL were selected as these compositions exhibited the most favourable balance of properties in the mould cured samples. Test specimens still attached to the print bed and illuminated under the UV light are shown in Fig. 3b. The printed sample containing 60% SIL exhibited the highest flexural modulus (11.78 ± 0.55 MPa) and ultimate compressive strength (10.69 ± 1.59 MPa). In contrast, the 80% SIL formulation demonstrated a substantial reduction in mechanical properties (Table S4), coinciding with a pronounced increase in ionic conductivity (Fig. 3), rising from 0.016 mS cm^{-1} at 60% SIL to 0.252 mS cm^{-1} at 80% SIL (Table S1). The 70% SIL sample provided an intermediate balance, exhibiting 0.043 mS cm^{-1} conductivity and moderate mechanical strength.

The additively manufactured SPEs demonstrated superior combined mechanical and electrochemical performance (Fig. 3c). Across all SIL content levels (60–80%), the printed samples consistently exhibited higher flexural modulus values, indicating enhanced mechanical robustness due to controlled spatial curing and more uniform resin network formation during the additive manufacturing process. Electrochemically, they also showed comparable, and in some cases improved, ionic conductivity. The 70% 3D printed sample achieved an 8% higher conductivity than equivalent mould-cured sample and 70% epoxy-based SPE from our previous work (Fig. 3c), suggesting the MSLA photocuring approach promotes not only better mechanical integration between phases but also maintains conductive ion channels within the resin matrix. The superior electrochemical and mechanical performance of the photocured SPEs over those produced using the RIM R935/H936 epoxy resin can be attributed in part to differences in mixing and curing methodologies. Assessment of the dimensional fidelity when printing the SPE was acceptable (Fig. S15). Although thin walls (<1 mm) began to collapse, they did not rupture, and circular voids (<1 mm) were printed with slightly smaller diameters than those specified in the model. As such, the simultaneous improvements in mechanical properties and ionic conductivity without significantly affecting printing resolution makes these SPEs promising for structural energy storage applications, where both properties are essential for effective multifunctional performance and tailored approach to design of such devices.

All samples were prepared using high shear mixing with integrated degassing, ensuring uniform dispersion of the SIL and consistent crosslinking throughout the polymer matrix.[22,23] The improved phase connectivity and structural coherence in the photocured systems, particularly the photocured variants, highlight the role of processing conditions in tailoring the SPE performance. Additionally, the anisotropic

© 2026 The Author(s). Co-published by the Institute of Process Engineering, Chinese Academy of Sciences and the Royal Society of Chemistry

Open Access Article. Published on 29 January 2026. Downloaded on 4/27/2026 7:11:15 PM.
This article is licensed under a Creative Commons Attribution-NonCommercial 3.0 Unported Licence.

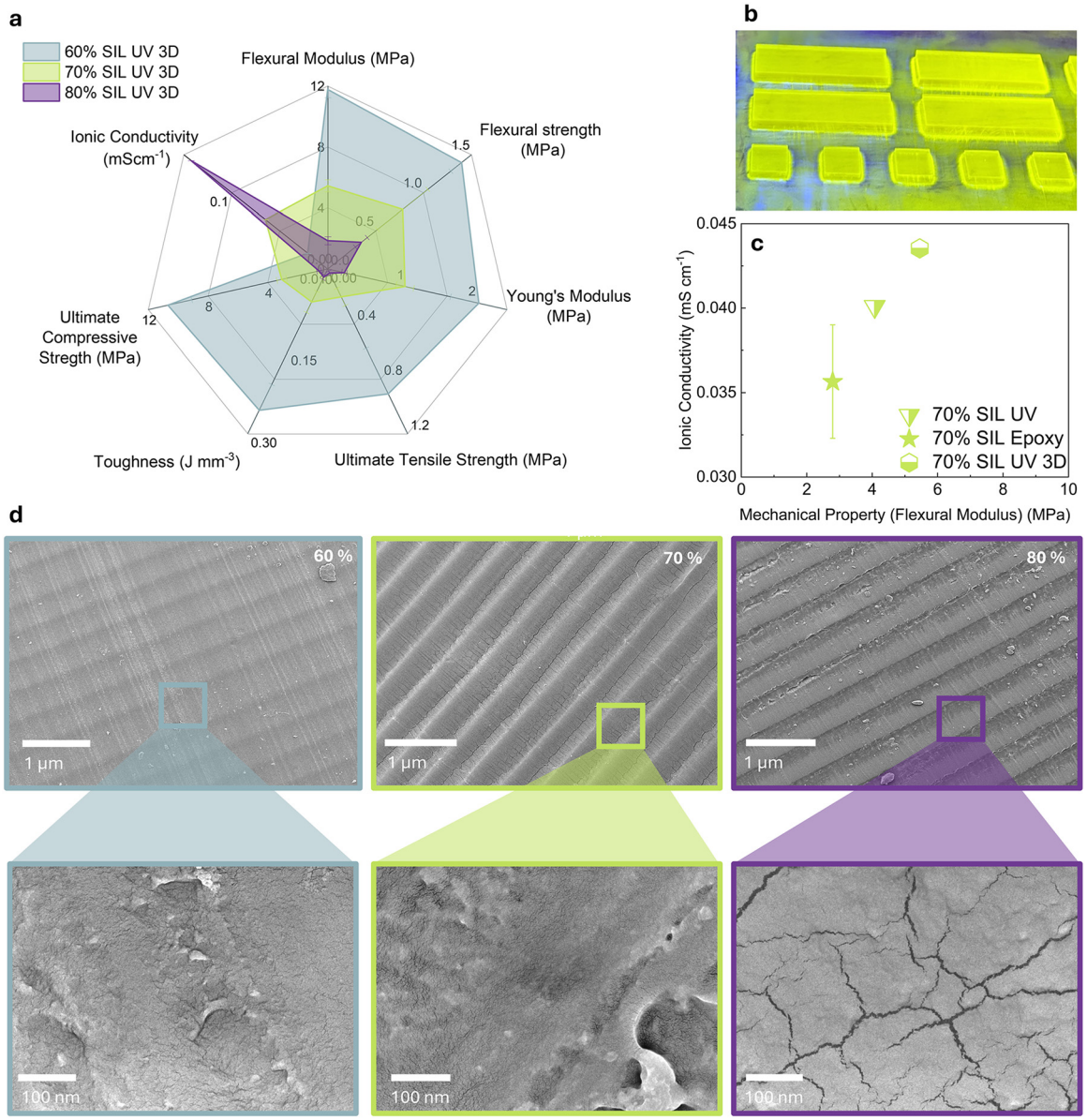

Fig. 3 (a) A radar chart showing the flexural, tensile and compressive mechanical properties and ionic conductivity electrochemical properties of 3D printed SPEs. Values available in the SI; (b) image of test specimens curing under a 400 W, 395 nm light source; (c) comparison of ionic conductivity and flexural modulus values (with standard deviation error bars) between this work's 3D printed 70% SIL SPE, mould-cured 70% SIL SPE from the proof-of-concept stage, and 70% SIL SPE based on thermosetting RIM R935/H936 resin from our previously published reports methodologies.[21,22] Data points represent the mean value, with standard deviation used for the error bars (N = 5); (d) SEM images of 60%, 70%, and 80% 3D printed SPEs, with inset images showing sections under higher magnification.

nature of the layer-by-layer process means parts are strongest within each deposited layer (the *XY* plane) and weakest perpendicular to those layers in the *Z* direction, where interlayer bonds tend to more readily fail under load, regardless of the fabrication method.[42–44] Consequently, orienting critical load-bearing axes parallel to the build plate and aligning infill rasters with those axes can partially mitigate but never fully eliminate this inherent anisotropy.[45]

SEM images of the printed samples reveal distinct and well aligned layers from the manufacturing process, indicating consistent layer deposition and good structural fidelity (Fig. 3d). In-plane alignment preferentially preserves continuous conductive pathways and yields higher effective capacitance and lower ESR. We observed modest anisotropy in our samples, with clear layer lines and solid interlayer bonding seen from SEM characterisation. Due to the high SIL loading in the tested SPEs, adhesion to the build plate would prevent fabrication of specimens with the mechanical loading axis not aligned with the build plane due to the prohibitively small surface area and contact needed for adhesion. Additionally, the SPE is orders of magnitude weaker compared to CF and any device-level mechanical performance would solely rely on the inherent strength of the fibres,

© 2026 The Author(s). Co-published by the Institute of Process Engineering, Chinese Academy of Sciences and the Royal Society of Chemistry

Open Access Article. Published on 29 January 2026. Downloaded on 4/27/2026 7:11:15 PM. This article is licensed under a Creative Commons Attribution-NonCommercial 3.0 Unported Licence.

with CF composites also exhibiting extensively-documented anisotropic behaviour and modes of failure.[46–48] While full elimination of this bias is not likely, as is common to all additive manufacturing methods, the main load-bearing performance would solely rely on the CF electrodes and not the SPE. Nevertheless, mitigations for SPE-level mechanical performance could include optimising exposure dose and overlap to ensure as full cure as possible at layer interfaces, reducing layer thickness to minimise interfacial defects, and using high energy post-cure annealing. Focus on a tailored approach to design that matches the end-use scenario in terms of load bearing distribution would have the highest impact to performance. Placement and shape then become more critical by designing component geometry and locating fibres so that CF-dominated load paths align with the primary service loads which is essential to achieving the required mechanical stability.

BJH gas sorption analysis was used to determine porosity of the SPE composition chosen for the fabrication of electrodes for the structural supercapacitor device. This method provides reliable pore size distribution and specific surface area measurements for mesoporous materials by analysing nitrogen adsorption/desorption isotherms and applying the BJH (Barrett–Joyner–Halenda) method to the adsorption branch to quantify the pore diameter in the 2–50 nm range, making it well suited to determine the porosity of the printed sample. As expected, a stochastic pore distribution was observed (Fig. S10), with most pores at 8.149 nm in diameter. With the 80% sample, the surface also exhibited extensive cracking, likely occurring from the removal of the SIL for SEM imaging, resulting in structural collapse of the polymer matrix.

A comprehensive thermal characterisation was also performed on both bulk-cured and additively manufactured samples with varying SIL contents to elucidate the influence of processing method on their structural and functional properties (SI Note: thermal analysis-TGA, DSC, TMA). In general, these data showed no significant change between SPE samples regardless of the fabrication method.

2.3 Piezoelectric response of the SPE

The photocured SPE was also evaluated for piezoelectric properties, to confirm viability of rapid prototyping of a trifunctional structural supercapacitor, enabling energy harvesting under externally applied mechanical force on the device. An SPE cylinder with the same dimensions as the internal opening of an aluminium holder was compressed, monitoring open circuit electric potential (OCP) and short circuit current in the process. Results showed a clear correlation between increasing force and OCP response (Fig. 4a), up to a maximum pressure of 0.7 MPa. After this, the OCP response showed exponential behaviour to the horizontal asymptote of maximum electric potential output, up to a maximum tested 1.77 MPa (Fig. S14). This behaviour indicates that the system's maximum electric potential output reaches the pressure limit of the generated electric potential due to the saturation of the induced crystallisation under these test conditions. However, current response increased at pressures over 0.7 MPa, indicating a drop in resistance since the voltage remained unchanged. Similar to our previously published reports,[40] a reduced pressure was applied directly after reaching the maximum pressure (Fig. 4a-250 seconds). It was observed that the output reduced from 1.89 V to 0.64 V when the pressure was reduced from 0.69 MPa to 0.18 MPa. This matches previous findings in neat ionic liquids from Hossain *et al.*[34,35] In our system, the SIL partly crystallises within the polymer and then redissolves when pressure is released. Thus, the output reflects the extent of crystallisation.

In our work, pressures reached a maximum of 1.77 MPa, with a linear pressure dependence up to 0.7 MPa (Fig. 4c). In the linear region electric potential increased by 3.03 V MPa^{-1} (R^2 = 0.994) and current at 1.62 μA MPa^{-1} (R^2 = 0.924) (Tables S11 and S12), which can still act as a piezoelectric energy harvesting system with reasonable resolution in an optimised electrical circuit with smoothing capacitors. Thus, making sensing capabilities plausible with the CF-based structural energy storage devices, with the maximum power density reaching 14.11 mW m^{-2} at a low 0.7 MPa (Fig. 4d) under these test conditions.

Melodia *et al.*[27] used [BMIM] cation to achieve 60x higher conductivity at the same IL wt% loading than this work, likely due to custom polymer formulation. In our system, boosting the SIL fraction to 70 wt% more than doubles the ionic conductivity (from 0.0160 to 0.0435 mS cm^{-1}, Table S1). Furthermore, piezoelectric response of these SPEs can synergistically improve the device performance *via* capturing ambient or supplied energy for self-charging purposes, which has been explored before in a thermosetting resin system.[10]

2.4 Direct printing of SPE on carbon fibre

Finally, the SPE was directly printed onto the surface-functionalised CF fabric (Fig. 5), simply by attaching it to the aluminium printing stage. A hexagonal patterned positive–negative snap fit design was employed to enable mechanical interlocking between the two electrodes. Following the integration of the current collectors, a separator-less supercapacitor was successfully assembled. The solid polymer electrolyte was stable up to 0.6 V (Fig. S1), which is adequate to harness the pseudocapacitive effect of the redox active DAQ and its carbonyl groups when covalently bound to the CF.[49] The experimental data showed a progressive and rapidly rising tail at higher electric potentials, indicating significant electrolyte decomposition and loss of stability beyond this limit. No change was detected in the stability even at higher operating temperatures (60 °C, Fig. S1), as expected due to degradation temperatures of 188.3 °C and 321.1 °C for the SIL and neat resin, respectively (Table S8).

The bulk of the observed capacitance arose from electrochemical double-layer formation (EDLC) at the electrode/electrolyte interface and pseudocapacitive contributions from the redox-active 2,6-diaminoanthraquinone covalently bound to

© 2026 The Author(s). Co-published by the Institute of Process Engineering, Chinese Academy of Sciences and the Royal Society of Chemistry

Open Access Article. Published on 29 January 2026. Downloaded on 4/27/2026 7:11:15 PM.
This article is licensed under a Creative Commons Attribution-NonCommercial 3.0 Unported Licence.

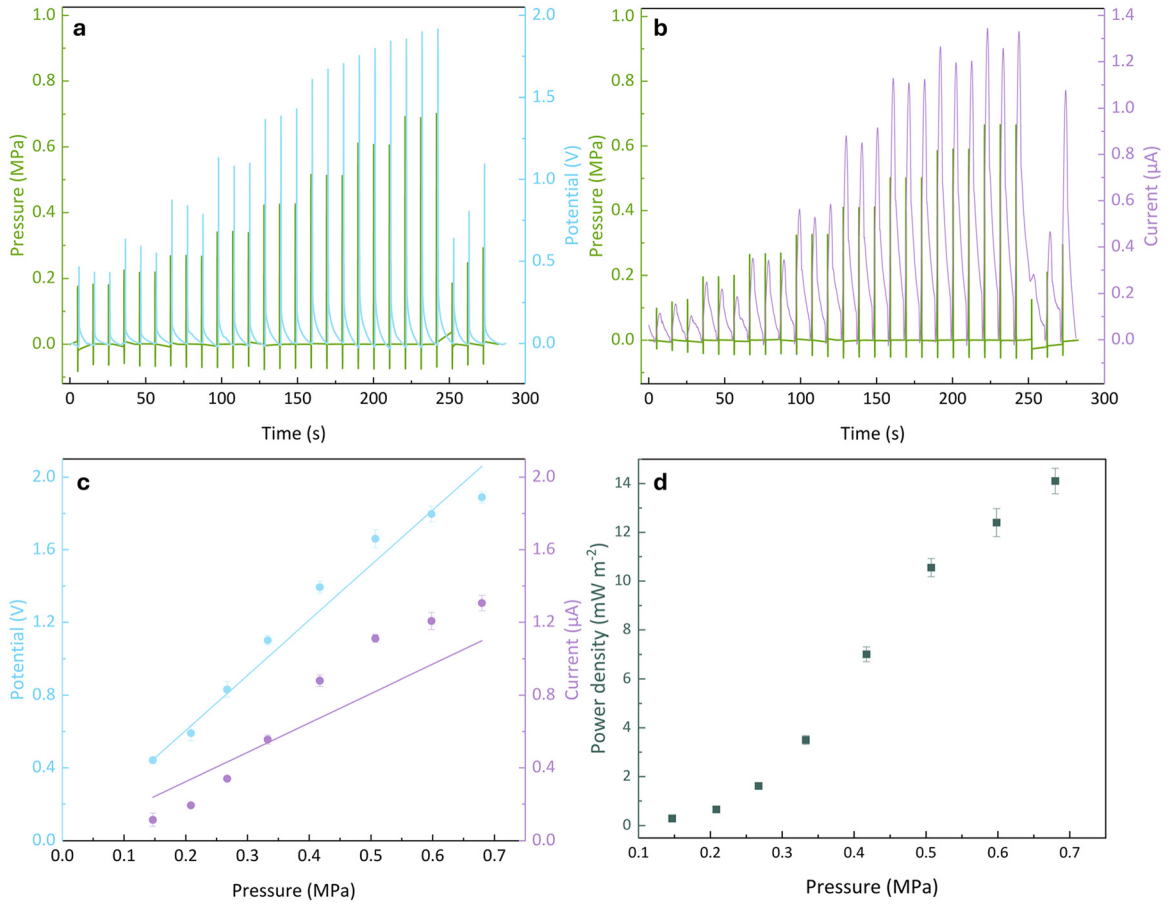

Fig. 4 Piezoelectric testing of 70% SIL UV 3D printed bicontinuous solid polymer electrolyte. (a) Double *y*-axis plot of pressure and electric potential over time; (b) double *y*-axis plot of pressure and current over time; (c) double *y*-axis plot of potential and current as a function of pressure. Data points represent the mean value, with standard deviation used for the error bars (N = 3). Details of line of best fit can be found in SI Note: piezoelectric testing; (d) power density plot as a function of pressure. Data points represent the mean value, with standard deviation used for the error bars (N = 3).

the CF surface. Electrochemical impedance spectra recorded before and after cyclic voltammetry revealed a slight increase in the charge-transfer resistance, consistent with the growth of a thin, resistive solid electrolyte interphase (SEI) on the electrode surface during cycling.

Thermal stability of the diazotised DAQ and functionalised CF was also investigated, which showed an onset of a distinct mass loss step of 40.52% at ~110 °C (Fig. S13c), corresponding to diazonium cleavage and nitrogen evolution reaction, as well as accompanying polymerisation with a sharp exothermic peak on the DSC trace. Onset of degradation reactions was then observed at 174 °C, roughly corresponding to the SIL degradation (Table S8). Conversely, such mass loss due to diazonium cleavage was not seen in the DAQ-functionalised CF due to the electrochemical reaction mechanism forming a radical by breaking this bond at the covalent attachment of DAQ onto CF step.[10,49]

This device showed modest performance (Fig. S3), however it was stable (Fig. S2), and its purpose as a proof-of-concept device is critical to the discussion and direction of

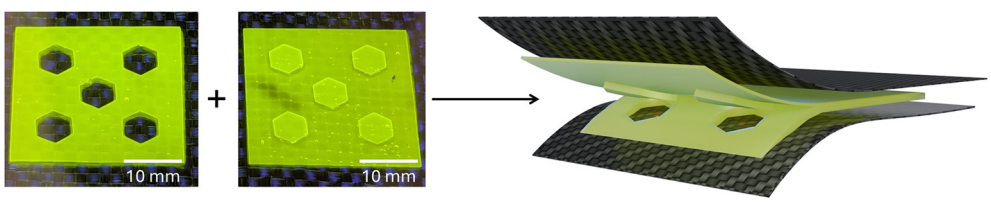

Fig. 5 Interlocking hexagonal SPE design on CF, under 400 W 395 nm UV light source, and a schematic of assembled supercapacitor device with the layers peeled open. Detailed electrochemical analysis of this device, including CV, GCD, EIS, fitted circuit, goodness-of-fit metrics, explanation, and parameters can be found in the SI Note: electrochemical characterisation.

© 2026 The Author(s). Co-published by the Institute of Process Engineering, Chinese Academy of Sciences and the Royal Society of Chemistry

Open Access Article. Published on 29 January 2026. Downloaded on 4/27/2026 7:11:15 PM.
This article is licensed under a Creative Commons Attribution-NonCommercial 3.0 Unported Licence.

future work in multifunctional (structural, energy harvesting, energy storage), scalable composites. Firstly, the device's 1 mm thick SPE served a dual role, both as the ion-conducting medium and as the physical separator between electrodes, eliminating the need for additional separators due to the manufacturing method locking the underlying CFs in place and protecting against stray fibre bridging the gap between electrodes. Separators often introduce manufacturing complexity, can be incompatible with electrode materials, as well as pose a delamination risk, leading to diminished device performance or premature failure and delamination. Secondly, the continuous liquid phase's energy harvesting capability is an unusual and peculiar function of this electrolyte which might warrant a trade-off in lower device-level energy storage performance if the piezoelectric energy can be harvested passively from converting the environmental stresses, such as vibration during high-speed motion or wind energy, into usable electrical energy to power devices such as sensors for structural health monitoring of composite structures.

Nevertheless, a photocured SPE printed directly on the functionalised CF electrodes presents itself as a viable rapid prototyping method for scalable energy storage device manufacture, limited only by the additive manufacturing machine's bed size in this case, enabling future optimisations in device topography for end-use scenarios. However, performance increases in energy storage can be achieved in many ways without compromising the ability of the electrolyte to act as an energy harvesting component. Apart from pore size, the relative amount and continuous nature of the polymer electrolyte is also a critical aspect. By coupling thermodynamic and kinetic controls during PIMS processing and adjusting resin composition (SIL : polymer ratio and monomer polarity) to change phase volume fraction and interfacial tension, the conductive phase can indeed become even more continuous. Additionally, polymer chemistry can be tuned *via* molecular weight changes or addition of compatibilisers to modulate conductivity and domain spacing, such as a low molecular weight block copolymer with a photocurable end and a conductive end (*e.g.*, PEO-*b*-PMMA).[50] The incorporation of additives or sacrificial templates such as nanoparticles or porogens would also enable fine-tuning of pore sizes.[51] However, a trade-off in ionic conductivity *versus* mechanical strength is still an inherent problem in this field, so optimisation requires balancing increased conductive phase/porosity for ion transport against retained mechanical integrity. Additionally, microstructuring of polymers would benefit from the incorporation of other polymerisation methods into the existing setup, such as RAFT to add agents that moderate chain growth, molecular weight distributions, end-group functionality and can also improve compatibility with ionic liquids or facilitate post-polymerisation modification.[27,28] On the processing side, a controlled local cure rate and exposure dose would lead to a faster cure which can achieve finer structures, whilst slower cure would favour larger pore formation. This could further be enhanced *via* voxel size variation, layer thickness and print orientation to affect local diffusion fields during cure, whilst designing features like microchannels directly in the CAD step could also expose an additional route to optimise through-thickness ion pathways for optimised ion transport and mechanical performance. This device is a proof-of-concept device to confirm feasibility of this scalable method of fabrication. As such, long-term testing, including variable temperature and humidity cycling, standardised impact and interlaminar toughness tests are required to fully establish their serviceability and quantify durability. Optimisation of SPE formulation and interlock geometry for both electrochemical and structural resilience in higher TRL devices is currently being considered for future works. Additionally, alternate methods of manufacture to incorporate UV-transparent optics, laser-based stereolithography and other projection systems are being explored to avoid LCDs, opening the broader UV-visible spectrum for photopolymerisation initiation.

3 Conclusions

This study demonstrates the application of masked stereolithography (MSLA) to fabricate acrylate-based thermoplastic bicontinuous solid polymer electrolytes (SPEs) incorporating a solvate ionic liquid (SIL) [Li-G3][TFSI] within a photocurable acrylate resin system. Through controlled layer-by-layer photopolymerisation, the printed SPEs exhibited markedly improved microstructural uniformity, mechanical performance, and ionic conductivity compared to mould-cured analogues. At 70 wt% SIL, the SPE fabricated *via* MSLA achieved an ionic conductivity of 0.0435 mS cm^{-1} alongside a flexural modulus of 6.71 MPa, outperforming both mould-cured and thermoset RIM R935/H936 epoxy-based SPEs reported previously. Additionally, this system was also piezoelectrically active, which under 1.77 MPa of pressure exhibited a stable maximum output of 2.02 ± 0.07 V and displaying a maximum power density of 14.11 mW m^{-2}. The electric potential responses demonstrated a strong linear correlation with applied pressure ($R^2 > 0.99$), highlighting its potential for integrated energy harvesting and sensing applications.

All fabrication was performed using a commercial resin and consumer-grade printer under ambient conditions, eliminating the need for an inert atmosphere, water exclusion, or specialised facilities. The SPEs were successfully printed directly onto functionalised CF electrodes, forming the first reported separator-less structural supercapacitor with a snap-fit, interlocking electrolyte architecture showing mechanical stability, intact ion conduction pathways, and facile device assembly by removing the need for discrete separators. Overall, this work presents a scalable, cost-effective, and accessible platform for producing multifunctional SPEs and related multifunctional systems with tuneable mechanical, electrochemical and, most importantly, piezoelectric properties of the SPE, and establishes a proof of concept towards rapid prototyping of structural energy storage and smart sensing within advanced composites and energy harvesting systems in one package.

© 2026 The Author(s). Co-published by the Institute of Process Engineering, Chinese Academy of Sciences and the Royal Society of Chemistry

Open Access Article. Published on 29 January 2026. Downloaded on 4/27/2026 7:11:15 PM. This article is licensed under a Creative Commons Attribution-NonCommercial 3.0 Unported Licence.

4 Experimental

4.1 Materials

Triglyme (G3) was purchased from Sigma-Aldrich (Merck Life Science Pty Ltd, Australia) and used as received without further purification. Lithium bis(trifluoromethanesulfonyl)imide (LiTFSI) was sourced from AA Blocks, Inc. (San Diego, USA) & Oakwood Products, Inc. (South Carolina, USA). SLA printer Sonic Mini 8K S and Aqua-Clear Resin were acquired from Phrozen (Phrozen Tech Co., Ltd., Taiwan). RIM R935/H936 resin was procured from Ironbark Composites (Torquay, Australia). A 395 nm 400 W ultraviolet (UV) lamp was used to cure mould cured samples.

4.2 Synthesis of solvate ionic liquids [Li-G3]TFSI

The synthesis of [Li(G3)][TFSI] SIL was carried out following standard methods for equimolar [Li(G3)][TFSI] preparation.[21,22] Lithium bis(trifluoromethanesulfonyl)imide and G3 (triglyme, triethylene glycol dimethyl ether) were combined in a 1 : 1 molar ratio, with the mixture stirred at room temperature for 48 hours. Afterward, it was subjected to drying under high vacuum at 140 °C for 1 hour to remove any remaining water. SIL water absence was confirmed using Karl Fischer titration on the 899 Coulometer (Metrohm, Switzerland), with the acceptable level for use considered at <10 ppm water content.

4.3 Synthesis of solid polymer electrolyte (SPE)

Mixtures of [Li(G3)][TFSI] SIL and Phrozen Aqua-Clear UV resin were prepared at the following weight ratios (SIL : resin) = 90 : 10, 80 : 20, 70 : 30, 60 : 40, and 55 : 45. Each formulation was homogenised using an ARE-250 planetary centrifugal mixer (Thinky U.S.A., Inc., Laguna Hills, USA) at 2000 rpm for 5 minutes. The resulting mixtures were immediately transferred into silicone moulds, kept wrapped in aluminium foil to prevent premature light exposure, then cured under a UV lamp for 5 minutes to produce mould-cured SPE samples for further testing. The mixing process was the same for the 3D printed SPE samples with the uncured SIL : resin solution being transferred to the printer rather than a mould. Further detail on the additive manufacturing settings is provided in the stereolithography (SLA) additive manufacturing experimental section.

4.4 Scanning electron microscopy (SEM)

The microstructures of the SPE samples were examined using a field emission scanning electron microscope JSM-7800F (Jeol, Ltd. Japan) set to an operating voltage of 5 kV. The samples were sputtered with a 5 nm gold coating with an ACE600 sputter coater (Leica Microsystems, Germany) to enhance conductivity.

4.5 Electrochemical characterisation

Electrochemical measurements were conducted using a VMP-300 electrochemical station (BioLogic, France) and Biologic EC-Lab v11.42 software in a two-electrode floating earth configuration at room temperature (17.5 ± 0.5 °C). Electrochemical impedance spectroscopy (EIS) was used to determine the ionic conductivity of SPEs, and the frequency range was scanned from 100 kHz to 100 mHz with 10 data points per decade and a sinusoidal amplitude of 10.0 mV. The sample blocks were placed between two polished copper plates within a battery testing clip. The electrochemical stability window was tested using cyclic voltammetry (CV) at 10 mV s^{-1} scan rate using a similar setup as for ionic conductivity testing.

The electrochemical performance of prototype supercapacitor devices was evaluated *via* cyclic voltammetry (CV), galvanostatic charge–discharge (GCD), and EIS measurements. All tests were performed in a two-electrode floating earth configuration under ambient conditions (17.5 ± 0.5 °C). Further experimental details, including the relevant equations used for data analysis, are provided in the SI Note: electrochemical characterisation.

4.6 Mechanical testing

4.6.1 Flexural testing. Flexural testing was performed using a load frame fitted with a 10 kN load cell (Instron 6800 Series Universal Testing System, Illinois Tool Works Inc., USA) using ASTM D2344/M specifications to ensure adequate data attainment and correct mode of failure. Seven specimens, each 35 mm long, 12 mm wide, and 4 mm thick, were positioned on a three-point bending setup with a 30 mm span between the support pins. A 10 mm diameter central roller applied the bending force at rates of 4 mm min^{-1}.

4.6.2 Tensile testing. Tensile testing was performed using a load frame fitted with pneumatic grips and a 1 kN load cell (Instron 5967 Series Universal Testing System, Illinois Tool Works Inc., USA), following the ASTM D638-22 (type V) method. At least 5 specimens were positioned in the pneumatic grips with a separation distance of 25.4 mm, and each specimen was measured individually, using the Bluehill Universal® v4.13 software. The strain rate was set to 1 mm min^{-1}. Air pressure was set to 25 psi for 55% SIL samples, with a gradual (linear) decrease to 18 psi for 80% to prevent compressive damage on the tabs of the specimen. The load and the associated displacement were recorded at a capture rate of 20 milliseconds which was used for stress–strain curve analysis.

4.6.3 Compression testing. Compression testing was conducted on a load frame fitted with a compression fixture and a 1 kN load cell (Instron 5967 Series Universal Testing System, Illinois Tool Works Inc., USA), following the ASTM D695-23. At least 5 specimens were tested by positioning them in the centre of the compressive fixture and a strain rate of 1 mm min^{-1} was applied. Specimen dimensions were 25.4 mm in height and 12.7 mm in width, but each specimen was measured using a set of callipers, which was entered at the time of testing in the software.

All tests were performed *via* the Bluehill Universal® v4.13 software. Further details on testing procedures and calculations are provided in the SI Note: mechanical testing.

© 2026 The Author(s). Co-published by the Institute of Process Engineering, Chinese Academy of Sciences and the Royal Society of Chemistry

Open Access Article. Published on 29 January 2026. Downloaded on 4/27/2026 7:11:15 PM. This article is licensed under a Creative Commons Attribution-NonCommercial 3.0 Unported Licence.

4.7 Thermal analysis

4.7.1 Thermomechanical analysis (TMA). TMA was performed with a 402 F1 Hyperion (Netzsch Group, Germany), which utilised a 4 mm diameter flat-tip pushrod for measuring expansion and compression. A steady force of 0.05 N was maintained on the sample during the tests. The samples were all cylindrical, with a diameter of 5 mm and a depth ranging from 3 to 3.5 mm and were compared against a fused silica control standard that measured 10 mm in height and 6 mm in diameter. Two Al_2O_3 sample spacers were used, each 6 mm in diameter. The temperature was gradually increased from −50 to 150 °C at a rate of 5 °C min^{-1} for all tests. The transitions for each sample were determined by identifying the minima in the derivative of the dL μm^{-1} *versus* temperature (°C) curve, which corresponded to the inflection points in the gradient. The average coefficient of linear thermal expansion for the resin samples was calculated between −30 °C and 30 °C, as specified in ASTM D696-16.

4.7.2 Thermogravimetric analysis (TGA). TGA experiments were carried out with a TG 209 F1 Libra instrument (Netzsch Group, Germany). The samples were prepared by cutting them for core usage in the TGA measurements. These measurements entailed heating the samples to 600 °C at a rate of 10 K min^{-1} whilst maintaining a nitrogen atmosphere. The temperature at which a 5% mass loss occurred above 150 °C was used to determine T_d (°C). This approach was adapted from the methodology described by Ueno *et al.*[52]

4.7.3 Simultaneous thermal analysis (STA). STA experiments were conducted on a STA 449 F5 Jupiter instrument (Netzsch Group, Germany). The diazotised DAQ powder was loaded into an open alumina crucible. DAQ-functionalised CF was tied into a knot and placed in a similar crucible. Both tests used a heating rate of 10 K min^{-1} under an argon atmosphere.

4.7.4 Differential scanning calorimetry (DSC). Differential scanning calorimetry (DSC) was conducted using a Netzsch Polyma DSC system with core sections extracted from dissected specimens, under a nitrogen environment. The thermal protocol involved heating the samples to 120 °C at a rate of 10 K min^{-1}, cooling them to −70 °C, holding for 5 minutes at that temperature, and then reheating from −70 °C to 120 °C for the second scan. Data from the second heating cycle was used for analysis, as the initial scan removes any prior thermal history of the material.

4.8 Surface functionalisation of woven carbon fibre

Toray FT300B (Toray Industries, Inc., Japan) plain woven CF fabric was desized *via* Soxhlet extraction with acetone at reflux for at least 48 h. The CF mat was then retrieved *via* vacuum filtration using a Büchner funnel and dried in a conventional oven for 1 hour. CF electrodes were manufactured *via* the use of electrochemical surface functionalisation of desized CF mats before directly using them as a substrate for additive manufacturing. A conductive copper tape (RS Components Pty Ltd, Australia) was applied to the long edge of a rectangular piece of the woven CF. Araldite was also applied to the copper-CF junction to prevent accidental copper contact with the electrografting solution. 2,6-Diaminoanthraquinone (DAQ) (CAS 131-14-6) was then covalently grafted onto CF electrochemically in a 3 electrode setup using potentiostatic cyclic voltammetry from 0 to −1.5 V at 10 mV s^{-1} for 20 cycles, with CF mat as the working electrode, leakless Ag/AgCl reference electrode (Model ET069, eDAQ Pty Ltd, Australia) and a 192 gsm non-woven CF mat G-TEX M (Gen 2 Carbon Ltd., Australia) as a counter electrode with a larger surface area. Grafting solution contained 10 mM of diazotised DAQ, all submerged in a grafting solution containing ACN : DMF in a v/v ratio of 19 : 1. This electrochemical grafting has been reported and experimentally confirmed in literature, resulting in covalent attachment to the CF surface and simultaneous increase in interfacial and capacitive properties.[49]

4.9 Masked stereolithography (MSLA) additive manufacturing

Samples were manufactured on Phrozen Sonic Mini 8k S SLA printer using the Phrozen Aqua-Clear resin at a layer height of 50 μm. For the neat resin samples manufacturer recommended profile was used with 6 bottom layers' exposure time of 15 seconds. All other layers had the exposure time set to 9 seconds, with 0.1 seconds of rest time after lift and 3 seconds of rest time after retraction. 7 millimetre lift distance was used, with a retraction speed of 180 mm min^{-1} for the first 5 millimetres of retraction and 90 mm min^{-1} for the last 2 millimetres. Exposure times alone were adjusted with the addition of SIL, determined by a series of experiments where UV light exposure was increased in 5 second increments, until even cure without deformation was observed. Briefly, identical resin, layer thickness, and light intensity was used, exposing each sample for progressively longer times in linear steps. After each exposure, samples were post-cured under 400 W 395 nm UV light source at 15 cm before detachment from the stage. Dimensional fidelity and layer adhesion were then evaluated using visual inspection and optical microscopy to determine the minimum exposure at which parts were considered fully cured. A safety margin was also added to account for variability in light output or resin batch differences, since the addition of the liquid SIL provided a heat sink effect and largely prevented significant rise in temperature in the SPE samples compared to neat resin samples. Bottom exposure time was ultimately set to 90 seconds for all SIL–resin mixtures. 60 wt% of SIL required an exposure time of 60 seconds, 70 wt% 75 seconds, and 80 wt% 90 seconds, regardless of printing surface (*i.e.*, either directly on aluminium stage or CF). If printed on CF, the woven mat was first attached to the aluminium stage in a dot grid pattern using the thermosetting resin West System 105/205 Fast Hardener (ATL Composites, Molendinar, Australia). UV resin infiltration through the CF mat increased the weight dramatically when saturated with uncured SPE, resulting in detachment from the aluminium stage during the inverted setup of the manufacturing process. Thus, necessitating the use of a thermoset pattern to ensure a flat planar configuration and

© 2026 The Author(s). Co-published by the Institute of Process Engineering, Chinese Academy of Sciences and the Royal Society of Chemistry

Open Access Article. Published on 29 January 2026. Downloaded on 4/27/2026 7:11:15 PM. This article is licensed under a Creative Commons Attribution-NonCommercial 3.0 Unported Licence.

adherence without compromising conductivity by forming an insulating layer on the expected electrode connection side of the CF mat.

4.10 Electrical analysis

To investigate the piezoelectric response, both potential and current outputs were monitored during mechanical compression tests. The sample was mounted in an aluminium holder with the internal mean diameter of 15 ± 0.14 mm, giving a mean surface area of 174.9 mm^2 and ensuring electrical contact *via* a copper wire. A PLA cylinder, embedded with a transverse copper wire was positioned in direct contact with the sample and inserted into the aluminium holder. The two copper electrodes were connected to separate data acquisition instruments for simultaneous voltage and current measurements.

Three distinct loading protocols were employed to assess the electromechanical response under varying compressive conditions. All tests were performed at a constant speed of 5 mm s^{-1}, with a 10 second rest interval between successive load steps. Each force increment was applied three times to ensure reproducibility ($N = 3$). In method 1, the applied load was initiated at 5 N and incrementally increased by 5 N up to a maximum of 80 N. Method 2 involved an initial force of 10 N, incremented by 10 N to a peak of 120 N, followed by immediate drop to 10, then 20 and finally 30 N. Method 3 applied compressive forces starting at 25 N with 25 N increments, reaching a maximum of 300 N.

4.10.1 Potential measurements. Open circuit potential (OCP) was recorded using an Autolab PGSTAT101 potentiostat (Metrohm, Switzerland). Data acquisition was carried out *via* the NOVA 2.1.8 software suite. The electric potential was measured continuously throughout the compression cycles to capture transient and steady-state voltage responses.

4.10.2 Current measurements. Current responses were measured using a 6514 System Electrometer (Keithley, USA) known for its high input impedance and low noise characteristics. Signal acquisition was performed using the e-corder 410 High-Resolution Data Recorder (eDAQ, Australia) in conjunction with eDAQ Chart software. The system was configured with an input range of ±2 V to accurately capture the low-current outputs.

4.11 Barrett–Joyner–Halenda (BJH) analysis

BJH was used to determine the pore size distribution, pore volume, and pore area of the additively manufactured SPE. The SPE with 70 wt% SIL was additively manufactured in a 10 × 5 cm rectangle at 150 μm layer height and the same parameters as described above in section 4.9. To prevent pore collapse, samples were washed in ethanol and water sequentially 5 times to remove the majority of the SIL from the pores. Full solvent exchange protocol was completed by keeping the samples in 1 L of deionized water for 4 days. After that, samples were frozen to −20 °C for 15 hours, followed by a freeze-drying cycle over 72 hours on the Martin Christ Beta 2-8 LSCbasic laboratory freeze dryer (Martin Christ Gefriertrocknungsanlagen GmbH, Germany) to remove water and keep the porous structure intact. A 12 mm quartz bulb tube without a rod was used for the gas sorption analysis. Samples were outgassed at 80 °C for 12 hours with a liquid nitrogen-cooled trap. Nitrogen gas adsorption isotherm was used for the BJH analysis with the Quantachrome® ASiQwin™ v5.21 software on the Quantachrome Autosorb iQ gas sorption analyzer (Quantachrome Instruments, Inc., Anton Paar GmbH, Germany).

4.12 Supercapacitor fabrication

A hexagonal interlocking design was employed (Fig. 5) at a final thickness of the SPE at 1 mm after assembly. Direct printing of the SPE onto the functionalised CF mat thus eliminated the need for a separator, since this method prevented generation of short circuit pathways between electrodes and would not pose a risk to the device. Electrodes were cut from the slightly larger CF mat in 35 × 35 mm squares and assembled by pairing the interlocking hexagonal features, with the SPE active area of the supercapacitor being 900 mm^2 (Fig. S5). Electrochemical testing was performed on the Biologic VMP-300 Electrochemical workstation (BioLogic, France). Full details and relevant equations can be found in the SI Note: electrochemical characterisation.

Author contributions

Žan Simon: conceptualisation, data curation, formal analysis, investigation, methodology, validation, visualisation, writing – original draft, writing – review & editing. Timothy Harte: conceptualisation, data curation, formal analysis, investigation, methodology, validation, visualisation, writing – original draft. Anna Demeraux: investigation, formal analysis, methodology, visualisation, writing – original draft. Ben Newman: conceptualisation, methodology, writing – review & editing. Piers Coia: investigation, methodology, writing – original draft. Nilupuli C. Rathnayaka: investigation, methodology. Daniel J. Eyckens: supervision, review & editing. Bhagya Dharmasiri: conceptualisation, data curation, formal analysis, investigation, methodology, validation, visualisation, writing – original draft, writing – review & editing, project administration, supervision. Luke C. Henderson: project administration, funding acquisition, supervision, resources, review & editing.

Conflicts of interest

The authors declare no conflict of interest.

Data availability

Data for this work is provided in the supplementary information (SI) and any additional or raw data is available upon reasonable request from the authors.

© 2026 The Author(s). Co-published by the Institute of Process Engineering, Chinese Academy of Sciences and the Royal Society of Chemistry

Open Access Article. Published on 29 January 2026. Downloaded on 4/27/2026 7:11:15 PM. This article is licensed under a Creative Commons Attribution-NonCommercial 3.0 Unported Licence.

Acknowledgements

The authors express their gratitude to Deakin University and the Australian Research Council (ARC) for their assistance *via* the Industry Transformation Research Hub (IH210100023), Discovery Projects (DP180100094, DP200100090, and DP230100587), and an IM Fellowship (IM230100048) for LH. Additional support was provided by the Office of Naval Research Global (N62909-22-1-2052). Research activities took place at the Deakin University Institute for Frontier Materials and the Carbon Nexus facilities. Furthermore, this study was funded by a Research Training Program (RTP) scholarship from the Australian Government. The authors acknowledge the facilities, and the scientific and technical assistance, of Microscopy Australia (formerly known as AMMRF) and the Australian National Fabrication Facility (ANFF). The authors also gratefully acknowledge the Deakin Electron Microscopy facility for support and assistance in this work.

References

1 G. Qi, Q. Cui, B. Zhang and S. Du, A carbon fiber lamina electrode based on macroporous epoxy with vertical ion channels for structural battery composites, *Compos. Struct.*, 2023, **304**, 116425.
2 P. Ladpli, R. Nardari, F. Kopsaftopoulos and F.-K. Chang, Multifunctional energy storage composite structures with embedded lithium-ion batteries, *J. Power Sources*, 2019, **414**, 517–529.
3 A. Javaid and M. Z. Ali, Multifunctional structural lithium ion batteries for electrical energy storage applications, *Mater. Res. Express*, 2018, **5**, 055701.
4 M. S. Siraj, S. Tasneem, D. Carlstedt, S. Duan, M. Johansen, C. Larsson, J. Xu, F. Liu, F. Edgren and L. E. Asp, Advancing structural battery composites: Robust manufacturing for enhanced and consistent multifunctional performance, *Adv. Energy Sustainability Res.*, 2023, **4**, 2300109.
5 J. Xu, C. Creighton, M. Johansen, F. Liu, S. Duan, D. Carlstedt, P. Mota-Santiago, P. Lynch and L. E. Asp, Effect of tension during stabilization on carbon fiber multifunctionality for structural battery composites, *Carbon*, 2023, **209**, 117982.
6 S. Duan, M. Cattaruzza, V. Tu, R. M. Auenhammer, R. Jänicke, M. K. G. Johansson, F. Liu and L. E. Asp, Three-dimensional reconstruction and computational analysis of a structural battery composite electrolyte, *Commun. Mater.*, 2023, **4**, 49.
7 T. Carlson, D. Ordéus, M. Wysocki and L. E. Asp, Structural capacitor materials made from carbon fibre epoxy composites, *Compos. Sci. Technol.*, 2010, **70**, 1135–1140.
8 E. S. Greenhalgh, S. Nguyen, M. Valkova, N. Shirshova, M. S. P. Shaffer and A. R. J. Kucernak, A critical review of structural supercapacitors and outlook on future research challenges, *Compos. Sci. Technol.*, 2023, **235**, 109968.
9 E. Senokos, D. B. Anthony, N. Rubio, M. C. Ribadeneyra, E. S. Greenhalgh and M. S. P. Shaffer, Robust single-walled carbon nanotube-infiltrated carbon fiber electrodes for structural supercapacitors: From reductive dissolution to high performance devices, *Adv. Funct. Mater.*, 2023, **33**, 2212697.
10 B. Dharmasiri, F. Stojcevski, K. A. S. Usman, S. Alex Qin, J. M. Razal, E. H. Doeven, P. S. Francis, T. U. Connell, Y. Yin, G. G. Andersson, A. Borkar and L. C. Henderson, Flexible carbon fiber based structural supercapacitor composites with solvate ionic liquid-epoxy solid electrolyte, *Chem. Eng. J.*, 2023, **455**, 140778.
11 R. C. Agrawal and G. P. Pandey, Solid polymer electrolytes: Materials designing and all-solid-state battery applications: An overview, *J. Phys. D: Appl. Phys.*, 2008, **41**, 223001.
12 Y. Xu, S. Pei, Y. Yan, L. Wang, G. Xu, S. Yarlagadda and T.-W. Chou, High-performance structural supercapacitors based on aligned discontinuous carbon fiber electrodes and solid polymer electrolytes, *ACS Appl. Mater. Interfaces*, 2021, **13**, 11774–11782.
13 N. Shirshova, A. Bismarck, S. Carreyette, Q. P. V. Fontana, E. S. Greenhalgh, P. Jacobsson, P. Johansson, M. J. Marczewski, G. Kalinka, A. R. J. Kucernak, J. Scheers, M. S. P. Shaffer, J. H. G. Steinke and M. Wienrich, Structural supercapacitor electrolytes based on bicontinuous ionic liquid–epoxy resin systems, *J. Mater. Chem. A*, 2013, **1**, 15300–15309.
14 S. J. Kwon, T. Kim, B. M. Jung, S. B. Lee and U. H. Choi, Multifunctional epoxy-based solid polymer electrolytes for solid-state supercapacitors, *ACS Appl. Mater. Interfaces*, 2018, **10**, 35108–35117.
15 A. Javaid, K. Ho, A. Bismarck, J. Steinke, M. Shaffer and E. Greenhalgh, Improving the multifunctional behaviour of structural supercapacitors by incorporating chemically activated carbon fibres and mesoporous silica particles as reinforcement, *J. Compos. Mater.*, 2018, **52**, 3085–3097.
16 S. Li, H. Jiang, T. Tang, Y. Nie, Z. Zhang and Q. Zhou, Improved electrochemical and mechanical performance of epoxy-based electrolytes doped with mesoporous TiO_2, *Mater. Chem. Phys.*, 2018, **205**, 23–28.
17 N. Shirshova, H. Qian, M. Houllé, J. H. G. Steinke, A. R. J. Kucernak, Q. P. V. Fontana, E. S. Greenhalgh, A. Bismarck and M. S. P. Shaffer, Multifunctional structural energy storage composite supercapacitors, *Faraday Discuss.*, 2014, **172**, 81–103.
18 V. Tu, L. E. Asp, N. Shirshova, F. Larsson, K. Runesson and R. Jänicke, Performance of bicontinuous structural electrolytes, *Multifunct. Mater.*, 2020, **3**, 025001.
19 W.-J. Cho, S.-K. Cho, J. H. Lee, J. H. Yoon, S. Kwon, C. Park, W. B. Lee, P. J. Yoo, M. Lee, S. Park, T. H. Kang and G.-R. Yi, Solid polymer electrolytes of ionic liquids via a bicontinuous ion transport channel for lithium metal batteries, *J. Mater. Chem. A*, 2023, **11**, 1676–1683.
20 T. Harte, B. Dharmasiri, Ž. Simon, D. J. Hayne, D. J. Eyckens and L. C. Henderson, Solvate ionic liquids: Past, present and future, *J. Mater. Chem. A*, 2025, **13**, 12746–12784.
21 T. Harte, B. Dharmasiri, D. J. Eyckens and L. C. Henderson, Closing the loop: Recyclable solvate ionic liquids in solid polymer electrolytes for circular economy, *ACS Sustainable Chem. Eng.*, 2024, **12**, 16114–16125.
22 T. Harte, B. Dharmasiri, P. Coia, D. J. Eyckens and L. C. Henderson, Bicontinuous solid polymer electrolytes using Li + enriched ionic liquids, *J. Mol. Liq.*, 2024, **402**, 124689.

© 2026 The Author(s). Co-published by the Institute of Process Engineering, Chinese Academy of Sciences and the Royal Society of Chemistry

Open Access Article. Published on 29 January 2026. Downloaded on 4/27/2026 7:11:15 PM. This article is licensed under a Creative Commons Attribution-NonCommercial 3.0 Unported Licence.

23 N. Hameed, D. J. Eyckens, B. M. Long, N. V. Salim, J. C. Capricho, L. Servinis, M. De Souza, M. D. Perus, R. J. Varley and L. C. Henderson, Rapid cross-linking of epoxy thermosets induced by solvate ionic liquids, *ACS Appl. Polym. Mater.*, 2020, **2**, 2651–2657.

24 J. Bae, S. Oh, B. Lee, C. H. Lee, J. Chung, J. Kim, S. Jo, S. Seo, J. Lim and S. Chung, High-performance, printable quasi-solid-state electrolytes toward all 3D direct ink writing of shape-versatile Li-ion batteries, *Energy Storage Mater.*, 2023, **57**, 277–288.

25 Z. Liu, X. Tian, M. Liu, S. Duan, Y. Ren, H. Ma, K. Tang, J. Shi, S. Hou, H. Jin and G. Cao, Direct ink writing of $Li_{1.3}Al_{0.3}Ti_{1.7}(PO_4)_3$-based solid-state electrolytes with customized shapes and remarkable electrochemical behaviors, *Small*, 2021, **17**, 2002866.

26 Q. Zhang, J. Zhou, Z. Chen, C. Xu, W. Tang, G. Yang, C. Lai, Q. Xu, J. Yang and C. Peng, Direct ink writing of moldable electrochemical energy storage devices: Ongoing progress, challenges, and prospects, *Adv. Eng. Mater.*, 2021, **23**, 2100068.

27 D. Melodia, A. Bhadra, K. Lee, R. Kuchel, D. Kundu, N. Corrigan and C. Boyer, 3D printed solid polymer electrolytes with bicontinuous nanoscopic domains for ionic liquid conduction and energy storage, *Small*, 2023, **19**, 2206639.

28 K. Lee, Y. Shang, V. A. Bobrin, R. Kuchel, D. Kundu, N. Corrigan and C. Boyer, 3D printing nanostructured solid polymer electrolytes with high modulus and conductivity, *Adv. Mater.*, 2022, **34**, 2204816.

29 B. R. Alandur Ramesh, B. Basnet, R. Huang, J. Jeong, H. Lee, T. Kyu and J.-W. Choi, The promise of 3D printed solid polymer electrolytes for developing sustainable batteries: A techno-commercial perspective, *Int. J. Precis. Eng. Manuf. Green Technol.*, 2024, **11**, 321–352.

30 M. Cheng and Y. Jiang, 3D-printed solid-state electrolytes for electrochemical energy storage devices, *J. Mater. Res.*, 2021, **36**, 4547–4564.

31 A. Vinegrad, H. Ragones, N. Jayakody, G. Ardel, M. Goor, Y. Kamir, M. M. Dorfman, A. Gladkikh, L. Burstein, Y. Horowitz, S. Greenbaum and D. Golodnitsky, Plasticized 3D-printed polymer electrolytes for lithium-ion batteries, *J. Electrochem. Soc.*, 2021, **168**, 110549.

32 D. W. McOwen, S. Xu, Y. Gong, Y. Wen, G. L. Godbey, J. E. Gritton, T. R. Hamann, J. Dai, G. T. Hitz, L. Hu and E. D. Wachsman, 3D-printing electrolytes for solid-state batteries, *Adv. Mater.*, 2018, **30**, 1707132.

33 S. Zekoll, C. Marriner-Edwards, A. K. O. Hekselman, J. Kasemchainan, C. Kuss, D. E. J. Armstrong, D. Cai, R. J. Wallace, F. H. Richter, J. H. J. Thijssen and P. G. Bruce, Hybrid electrolytes with 3D bicontinuous ordered ceramic and polymer microchannels for all-solid-state batteries, *Energy Environ. Sci.*, 2018, **11**, 185–201.

34 M. I. Hossain and G. J. Blanchard, Ionic liquids exhibit the piezoelectric effect, *J. Phys. Chem. Lett.*, 2023, **14**, 2731–2735.

35 M. I. Hossain, H. Wang, L. Adhikari, G. A. Baker, A. Mezzetta, L. Guazzelli, P. Mussini, W. Xie and G. J. Blanchard, Structure-dependence and mechanistic insights into the piezoelectric effect in ionic liquids, *J. Phys. Chem. B*, 2024, **128**, 1495–1505.

36 Y. Yoshimura, T. Takekiyo, Y. Imai and H. Abe, Pressure-induced spectral changes of room-temperature ionic liquid, N,N-diethyl-N-methyl-N-(2-methoxyethyl)ammonium bis(trifluoromethylsulfonyl)imide, [DEME][TFSI], *J. Phys. Chem. C*, 2012, **116**, 2097–2101.

37 Y. Yoshimura, H. Abe, Y. Imai, T. Takekiyo and N. Hamaya, Decompression-induced crystal polymorphism in a room-temperature ionic liquid, N,N-diethyl-N-methyl-N-(2-methoxyethyl) ammonium tetrafluoroborate, *J. Phys. Chem. B*, 2013, **117**, 3264–3269.

38 T. Takekiyo and Y. Yoshimura, Peculiar high-pressure phase behavior of 1-butyl-3-methylimidazolium iodide, *J. Phys. Chem. B*, 2020, **124**, 7659–7667.

39 L. Su, M. Li, X. Zhu, Z. Wang, Z. Chen, F. Li, Q. Zhou and S. Hong, In situ crystallization of low-melting ionic liquid [BMIM][PF_6] under high pressure up to 2 GPa, *J. Phys. Chem. B*, 2010, **114**, 5061–5065.

40 Ž. Simon, B. Dharmasiri, T. Harte, P. C. Sherrell and L. C. Henderson, From stress to charge: Investigating the piezoelectric response of solvate ionic liquid in structural energy storage composites, *Mater. Horiz.*, 2024, **11**, 4321–4328.

41 T. Harte, B. Dharmasiri, G. S. Dobhal, T. R. Walsh and L. C. Henderson, Accelerated lithium-ion diffusion via a ligand 'hopping' mechanism in lithium enriched solvate ionic liquids, *Phys. Chem. Chem. Phys.*, 2023, **25**, 29614–29623.

42 A. Hendlmeier, Ž. Simon, Y. A. Wickramasingha and L. C. Henderson, A comparison of compression molded and additively manufactured short carbon fiber reinforced polyamide-6 samples and the effect of different infill printing patterns, *Polym. Compos.*, 2021, **42**, 4728–4735.

43 A. Z. Farkas, S.-V. Galatanu and R. Nagib, The influence of printing layer thickness and orientation on the mechanical properties of DLP 3D-printed dental resin, *Polymers*, 2023, **15**, 1113.

44 E.-H. Lee, J.-S. Ahn, Y.-J. Lim, H.-B. Kwon and M.-J. Kim, Effect of layer thickness and printing orientation on the color stability and stainability of a 3D-printed resin material, *J. Prosthet. Dent.*, 2022, **127**, 784.e1–784.e7.

45 E. Wang, F. Yang, X. Shen, Z. Li, X. Yang, X. Zhang and W. Peng, Investigation and optimization of the impact of printing orientation on mechanical properties of resin sample in the low-force stereolithography additive manufacturing, *Materials*, 2022, **15**, 6743.

46 J. Wang, N. Salim, B. Fox and N. Stanford, Anisotropic compressive behaviour of turbostratic graphite in carbon fibre, *Appl. Mater. Today*, 2017, **9**, 196–203.

47 D. Jiang and D. E. Smith, Anisotropic mechanical properties of oriented carbon fiber filled polymer composites produced with fused filament fabrication, *Addit. Manuf.*, 2017, **18**, 84–94.

48 A. N. Ruslantsev, Y. M. Portnova, L. P. Tairova and A. M. Dumansky, Analysis of mechanical properties anisotropy of

© 2026 The Author(s). Co-published by the Institute of Process Engineering, Chinese Academy of Sciences and the Royal Society of Chemistry

Open Access Article. Published on 29 January 2026. Downloaded on 4/27/2026 7:11:15 PM.
This article is licensed under a Creative Commons Attribution-NonCommercial 3.0 Unported Licence.

nanomodified carbon fibre-reinforced woven composites, *IOP Conf. Ser.: Mater. Sci. Eng.*, 2016, **153**, 012003.

49 P. Coia, B. Dharmasiri, F. Stojcevski, D. J. Hayne, E. Austria, B. Akhavan, J. M. Razal, K. A. S. Usman, M. K. Stanfield and L. C. Henderson, Scalable electrochemical grafting of anthraquinone for fabrication of multifunctional carbon fibers, *J. Mater. Sci. Technol.*, 2024, **200**, 162–175.

50 Q. Xiao, X. Wang, W. Li, Z. Li, T. Zhang and H. Zhang, Macroporous polymer electrolytes based on PVDF/PEO-b-PMMA block copolymer blends for rechargeable lithium ion battery, *J. Membr. Sci.*, 2009, **334**, 117–122.

51 M. H. Mohamed and L. D. Wilson, Porous copolymer resins: Tuning pore structure and surface area with non reactive porogens, *Nanomaterials*, 2012, **2**, 163–186.

52 K. Ueno, K. Yoshida, M. Tsuchiya, N. Tachikawa, K. Dokko and M. Watanabe, Glyme–lithium salt equimolar molten mixtures: Concentrated solutions or solvate ionic liquids?, *J. Phys. Chem. B*, 2012, **116**, 11323–11331.

© 2026 The Author(s). Co-published by the Institute of Process Engineering, Chinese Academy of Sciences and the Royal Society of Chemistry